This is the preprint manuscript of the article that appeared in final form in *Journal of Materials Chemistry A*, 2023, **11**. 20506-20517, which has been published in final form at **https://doi.org/10.1039/d3ta03791f**.

Unravelling the electrochemical activation and the reaction mechanism of *maricite*-$NaFePO_4$ using multimodal *operando* techniques

Carlos Berlanga,[ab] Moulay Tahar Sougrati,[cd] Antonio J. Fernández-Ropero,‡[a] Neyrouz Baaboura,[a] Nicholas E. Drewett,[a] Juan M. Lopez del Amo,[a] Gene Nolis,[a] Jose S. Garitaonandia,[e] Marine Reynaud,[a] Lorenzo Stievano,[cd] Montse Casas-Cabanas*[af] and Montse Galceran*[a]

[a] Center for Cooperative Research on Alternative Energies (CIC energiGUNE), Basque Research and Technology Alliance (BRTA), Parque Tecnológico de Álava, Albert Einstein, 48, 01510, Vitoria-Gasteiz, Spain.
E-mail: mgalceran@cicenergigune.com; mcasas@cicenergigune.com
[b] Departamento de Química Inorgánica, Universidad del País Vasco UPV/EHU, P.O. Box 644, 48080 Bilbao, Spain
[c] ICGM, Univ. Montpellier, CNRS, ENSCM, Montpellier, France
[d] RS2E, CNRS, Amiens, France
[e] Departamento de Física. Facultad de Ciencia y Tecnología. Universidad del País Vasco (UPV/EHU) P.O. Box 644, 48080 Bilbao, Spain
[f] IKERBASQUE, Basque Foundation for Science, 48013 Bilbao, Spain
‡ Current address of Antonio J. Fernánndez-Ropero: antoniof@ing.uc3m.es

Abstract

The electrochemical properties of maricite $NaFePO_4$ can be triggered by ball milling with carbon. The origin of such activation is still unclear, as this material does not exhibit apparent open channels for Na^+ diffusion. Herein, a characterisation approach including several complementary techniques is applied to investigate the effect of ball milling on the structure of maricite $NaFePO_4$ prepared by hydrothermal synthesis, and how these modifications influence its electrochemical mechanism. Our findings confirm the partial nanosizing and amorphisation of maricite, going along with the oxidation of the iron centres during ball milling, and allow the elucidation of different mechanisms contributing to the total capacity delivered during (de)sodiation. Although only 15% of the capacity is explained by Na^+ insertion/extraction in/from bulk crystalline $NaFePO_4$, 75% of the total capacity is attributed to the simultaneous Fe^{3+}/Fe^{2+} redox activity. The remaining 25% extra-capacity does not seem to be related to Fe^{3+}/Fe^{2+} activity, but rather to surface activity, associated with the new species formed during ball milling.

Introduction

$NaFePO_4$ (NFP), a widely studied cathode material for sodiumion batteries, exhibits a noticeable theoretical capacity of 154 mA h g^{-1}, corresponding to the extraction/insertion of one sodium per unit formula [1–5]. This compound crystallizes

into two different structures: triphylite and maricite (both of them derived from the parent olivine structure) [6]. The triphylite form offers excellent long-term cyclability despite the substantial volumetric change associated with Na^+ (de)intercalation (*ca*.17%) [1,5,7–9]. Apart from the moderate average voltage, its main drawback is its metastable nature, as this polymorph can onlybe prepared by chemical or electrochemical ion exchange from its lithiated counterpart $LiFePO_4$. In fact, maricite is the thermodynamically stable form obtained by common synthetic routes. The structure of maricite resembles to that of triphylite, albeit with Na and Fe atoms having exchanged positions, resulting in a structure with no apparent open channels for Na^+ diffusion. In several previous reports, the poor electrochemical activity of maricite, with practical capacities typically below 30 mA h g^{-1}, was attributed to such a lack of Na^+ diffusion paths [10,11].

Surprisingly, Kim *et al.* reported a reversible capacity of 142 mAh g^{-1} at 0.05C with a capacity retention of 95% after 200 cycles [12]. These results created much interest in the community and more recent works also reported a dramatic improvement of the capacity of maricite, nearly reaching its theoretical value, when the material is nanosized by ball milling or amorphized. Liu *et al*. reported the preparation by electrospinning of maricite NFP nanodots (~ 1.6 nm in size) delivering a reversible capacity of 145 mA h g^{-1} at 0.2C with a capacity retention of nearly 89% over 6300 cycles [13]. Other works also explored the enhancement of the electrochemical properties through the activation of the material by mechanochemical treatments [14,15]. Another strategy to enhance the electrochemical properties of maricite was proposed by Liu *et al*., who prepared highly dispersed maricite NFP nanoclusters with ultrafine NFP@C subunits (~3 nm), delivering a capacity of ~149 mA h g^{-1} at 0.2 C, and with a superior cycling performance (~91 mA h g−1 at 10 C after 5000 cycles with a capacity retention of 95%) [16]. Several hypotheses have been proposed for such unexpected findings, although a unifying rationalization has yet to be provided to date.

Possible explanations suppose that the material undergoes a partial irreversible amorphization or becomes locally disordered during the first charge process, which would be in agreement with the change in the voltage profile between the first charge and the subsequent electrochemical cycles [12,13,16,17]. Other authors reported the introduction of some structural disorder in the pristine crystal structure by ball milling [14]. More recently, Xiaong *et al.* attributed the origin of this electrochemical enhancement to the evolution of the local structure of Fe centres from edge-sharing FeO_6 octahedra to FeO_n polyhedral [15]. Nevertheless, such partially amorphised or disordered structure, which would result in a lower activation energy for Na^+ diffusion in the solid, would be driven by the transformation from maricite to triphylite since heterosite $FePO_4$ (analogue to triphylite) is more stable than maricite $FePO_4$ [12]. However, independent of the activation mechanism, maricite NFP exhibits a different first charge voltage profile, which delivers a lower capacity than the subsequent ones.

Other authors proposed a pseudocapacitive mechanism in several related compounds such as crystalline maricite $NaMPO_4$ (M = Co, Mn, Ni) tested in aqueous electrolytes or $NaMn_{1/3}Ni_{1/3}Co_{1/3}PO_4$, although the expected rectangular curve typical of an ion adsorption mechanisms was observed only for $NaMnPO_4$ and $NaNiPO_4$ [18,19].

The electrochemical reaction mechanism of maricite NFP is, thus, still a matter of debate. Confusion is further aggravated by the different degrees of crystallinity/disorder degree/amorphicity reported for the different studied materials, in some cases related only to the broadening of diffraction peaks, in other ones to the appearance of a large diffuse background in the X-ray diffraction (XRD) pattern, and in some evidenced by the total disappearance of the crystalline reflections. Indeed, these definitions are arbitrarily used in different situations, and often distinguishing between a material with reduced periodic length (*i.e.*, small crystallites) and a material that totally lacks long range order is not straightforward [12,13,15,16].

Motivated by the broad discussion and in order to provide some clarity regarding this topic, we carried out an in-depth study to better understand the electrochemical behaviour of maricite NFP. This work was carried out by applying complementary lab-scale and high resolution XRD, as well as ^{57}Fe Mössbauer, Raman, and X-Ray Absorption (XAS) spectroscopy either *ex situ* or *in situ* and, when possible, under *operando* conditions, to investigate the impact of the ball milling pre-treatment at both surface and bulk level and the reaction mechanism of maricite NaFePO4 *vs*. Na metal. Our findings show that during the ball milling the sample is partially amorphized and oxidized, which contributes to the enhancement of the electrochemistry performance.

Experimental

Synthesis of maricite NaFePO4

Maricite $NaFePO_4$ was synthesised *via* a hydrothermal route. Excess of NaOH (Sigma Aldrich 97%) and stoichiometric amounts of $FeSO_4{\cdot}7H2O$ (Sigma Aldrich, 99%) and H_3PO_4 (Alfa Aesar, 85%) were dissolved in water. This mixture was transferred in a glass liner, the autoclave was sealed and heated at 200°C for 4 hours. The obtained precipitate was filtered, washed, and dried in oven at 60°C. A white-beige powder of maricite $NaFePO_4$ was obtained.

This solid was mixed with C65 carbon in a ratio of 80:20 and milled in a PULVERISETTE 5 (Fristsch) planetary ball mill in order to increase the conductivity as well as to reduce the particle size. The mill was operated at 200 rpm with a ball:sample mass ratio of 40:1. The effect of the ball milling time was evaluated for different times of treatment: 3, 6, 9 and 12 hours. These samples are named NFP_Xh, where X is the ball milling

time. Sample NFP_0h represents pristine maricite NFP, without milling and without addition of carbon C65.

Synthesis maricite carbon coated NaFePO4 from triphylite carbon coated NaFePO4

Triphylite carbon coated $NaFePO_4$ (*t*-*cc*-NFP) cathode material was synthesized by chemical delithiation and subsequent chemical sodiation of commercial $LiFePO_4$ as it was reported in a previous paper [1]. Then the *t*-cc-NFP was heated at 500°C for 6h in order to obtain the carbon coated maricite NFP (*cc*-*m*-NFP) [5]

Characterization techniques

XRD patterns were collected using a Bruker D8 Discover X-ray diffractometer equipped with a LYNXEYE XE detector with the Cu Kα radiation (λ = 1.5418 Å) in the 2θ range 10−80°. Le Bail refinements were performed using the FullProf Suite [20] in order to determine the unit cell parameters.

The amount of Na, Fe and P in the targeted composition was determined by inductively coupled plasma atomic emission spectroscopy (ICP-AES, Horiba Yobin Yvon Activa). Solutions of appropriate concentrations for elemental analysis were prepared from a mother solution obtained by digesting 10 mg of synthesized material in 20 mL HCl (diluted from 20% in volume), and heating at 190°C for 15 minutes.

The homogeneity and morphology of the samples were examined by scanning electron microscopy (SEM) using a FEI - QUANTA 200FEG microscope equipped with energy-dispersive X-ray spectroscopy (EDS).

Raman spectra were recorded at room temperature with a Raman microscope (Renishaw inVia), using a 633 nm wavelength laser focused through an inverted microscope (Leica), via a 50x objective (Leica).

O and Na K-edge, as well as Fe $L_{2,3}$-edge XAS measurements were carried out at BL29-BOREAS beamline (Synchrotron Alba, Spain) in both total electron yield (TEY) and fluorescence yield (FY) detection modes. Signals from TEY mode correspond to the chemical state of the surface layer of the material, whereas FY corresponds to the signal of elements contained in a layer of approximately 100 nm into the material. Thus, considering the particle size of the studied materials, the FY signals can be considered as representative of the bulk structure.

Magic Angle Spinning Nuclear Magnetic Resonance (MAS NMR) experiments were performed at 52.9 MHz, on a Bruker-300 spectrometer charged to a field of 4.7 T using a 1.3 mm MAS probe at rotor spinning speed of 50 kHz. A rotor synchronized spin−echo pulse sequence (90°−τ−180°−τ1−acquisition) was used with typical 90° and 180° pulses of 1.2 and 2.4 µs for ^{23}Na and 1.5 and 4 µs, for ^{31}P respectively. Recycle day

of 1s was used for all experiments. The number of scans was set to 4k for ^{23}Na and 6k for ^{31}P experiments.

^{57}Fe Mössbauer spectra were measured at room temperature (293 K) with a ^{57}Co:Rh source and a Kr gas proportional counter. The spectrometer was operated with a triangular velocity waveform, and the spectra were fitted with superpositions of appropriate sets of the Lorentzian lines using NORMOS program for powder measurement and PC-MOS computer program for operando measurements [21,22]. Isomer shift values are given relative to α-Fe metal. In the *operando* Mössbauer spectroscopy measurements, the cell was cycled between 4.5 and 1.5 V vs. Na^+/Na. The Mössbauer absorbers were prepared as self-standing electrodes of maricite $NaFePO_4$ (previously ball milled with C65, NFP_12h) mixed with PTFE binder and mounted in a specifically designed *in situ* electrochemical cell [23]. The data of the *operando* experiment were analysed globally using a chemometric approach using Principal Component Analysis (PCA) and Multivariate Curve Resolution with the Alternating Least Squares algorithm (MCR–ALS), via a procedure described in detail by Fehse *et al* [24]. This analysis allows the extraction of the pure spectral components necessary to describe, via adapted linear combinations, the entire spectral dataset. Such components were finally analysed as normal Mössbauer spectra as described above.

Synchrotron XRD (SXRD) experiments were performed at the BL04-MSPD beamline at ALBA facilities to obtain high-intensity and high resolution data with low acquisition times (3 minutes). *Operando* patterns were collected at a wavelength λ = 0.825890 Å using our homemade *operando* electrochemical cell equipped with a Beryllium (Be) window as a current collector and using a transparent plunger also equipped with a Be window for transmission geometry [25]. Electrode discs were prepared by mixing maricite $NaFePO_4$ with carbon C65 (Imerys) in a ratio of 62:38 using Whatman GF/D borosilicate glass as separator, a 1.0 M sodium hexafluorophosphate ($NaPF_6$, Sigma-Aldrich) in a 1:1 vol. mixture of ethylene carbonate (EC, Acros) and dimethyl carbonate (DMC) as electrolyte and high purity Na metal (Sigma-Aldrich) as negative electrode. The *operando* cell was cycled in the galvanostatic mode at C/20 in the voltage window of 4.5 – 1.5 V vs Na^+/Na using an SP200 Biologic potentiostat. Rietveld refinements of the operando SXRD patterns were performed with the FullProf software as described above, by following the evolution of both unit cell parameters and atomic occupancies.

Electrochemical analysis

The electrochemical investigations of hand milled $NaFePO_4$ simply mixed in a mortar with C65 (NFP_0h) and ball milled $NaFePO_4$/C65 (NFP_3h, NFP_6h, NFP_9h and NFP_12h) mixtures were carried out in CR2032 coin cells. The active material $NaFePO_4$/C65 (80:20) was mixed with C65 carbon additive and [poly(vinylidene difluoride)] (PVdF) binder in a mass ratio of 85:10:5 in *N*-methyl-2-pyrrolidone (NMP).

The final ratio was 68:27:5 (active material:C65:PVdF). The slurry was cast on an aluminium current collector and dried overnight at 120°C under vacuum. Electrode disks were punched and pressed at 5 ton before assembling the coin cells. Half cells were assembled using Whatman GF/D borosilicate glass, a 1.0 M solution of $NaPF_6$ in 1:1 vol. EC:DMC and high purity Na metal as a separator, electrolyte and negative electrode, respectively. The cells were charged and discharged in the galvanostatic mode at C/20 in the voltage range 4.5 – 1.5 V vs. Na^+/Na.

Results and discussion

Effect of ball milling

Maricite NaFePO4 was synthesized by the hydrothermal route. All the peaks of the XRD pattern of the as-synthesized sample (NFP_0h), shown in Figure 1, can be indexed in the orthorhombic system with *Pnma* space group. No impurities are detected by XRD. The cell parameters, obtained from Le Bail refinement, *a* = 8.9959(9) Å, *b* = 6.8617(8) Å and *c* = 5.0459(6) Å are in agreement with previous literature data [26]. The sample presents a good homogeneity (Figure SI1), with agglomerates of stick-shaped particles: single particles have a homogeneous width of ~800 nm and a length ranging from 1 to 8 µm, while the crystallite size estimated from the Le Bail refinement is 170 nm, which is indicative of a polycrystalline material. ICP and EDS analyses indicate a Na:Fe:P ratio of 1:1:1, corresponding to the theoretical one. In addition, Mössbauer spectroscopy reveals that the pristine maricite NFP_0h contains only Fe^{2+} (Figure SI2), as expected.

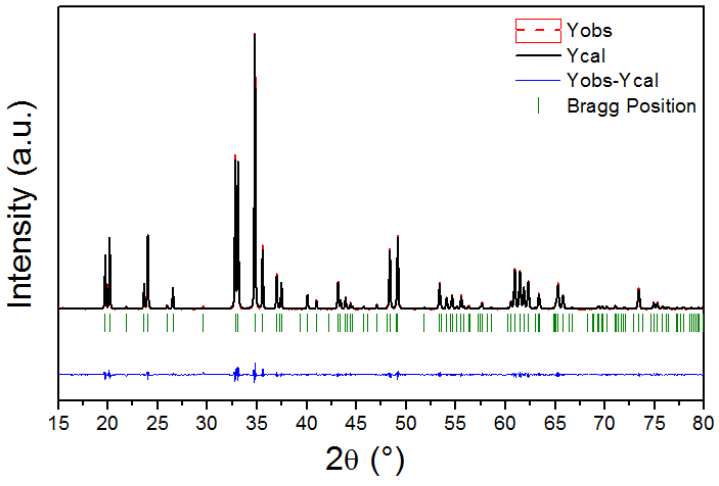

Figure 1. *Le Bail refinement of the pure maricite NaFePO4 obtained by hydrothermal synthesis (NFP_0h sample).*

The first charge/discharge galvanostatic cycle of NFP_0h (NFP without ball milling with carbon) vs. Na^+/Na metal is shown in Figure 2. As expected, the battery delivers only a

low capacity of 21 and 13 mAh g^{-1} in the first charge and discharge, respectively. This poor performance is attributed to the large particle size, the low conductivity of $NaFePO_4$, and/or the lack of Na^+ diffusion channels, as already discussed in the introduction [11,27].

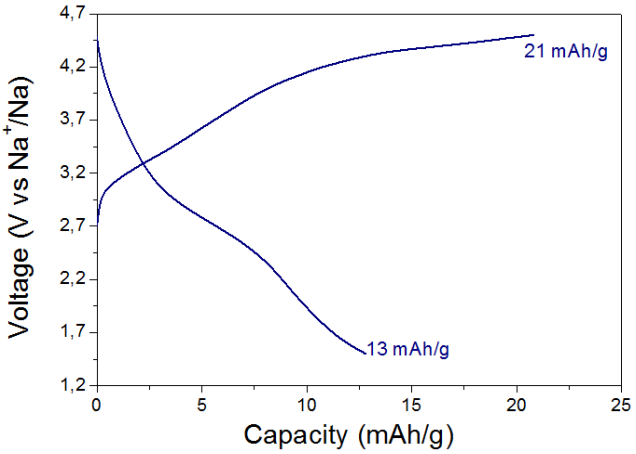

Figure 2. *First charge and discharge curve of pristine maricite $NaFePO_4$ obtained by hydrothermal synthesis (NFP_0h sample). The active material NFP was hand mixed with C65.*

As shown in previous works [12,13,16] ball milling maricite $NaFePO_4$ with carbon to increase the conductivity and decrease the particle size effectively improves the electrochemical performance. With this in mind, we studied the effect of different milling times (3, 6, 9 and 12 hours) on the structure, the particle size, the morphology and the electrochemical performance. Figure 3 shows the evolution of the XRD

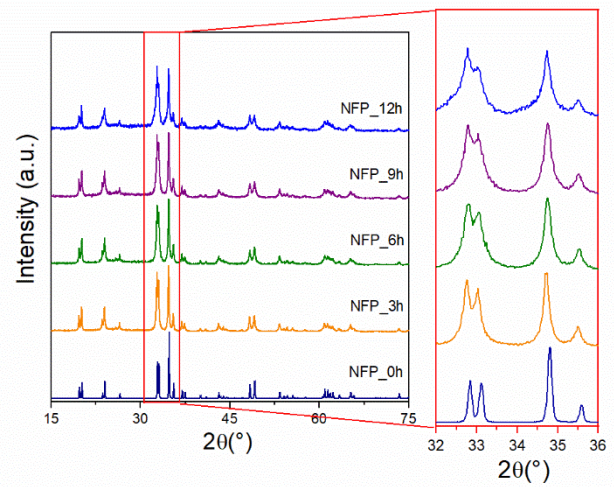

Figure 3. *XRD patterns of NaFePO4/C obtained by hydrothermal synthesis (NFP_0h) and at different ball milling times (NFP_xh).*

patterns with milling time. In all cases, only pure maricite NFP is detected with similar unit cell parameters (Table SI1). After 3h of ball milling, a substantial broadening of the diffraction peaks, corresponding to a significant decrease of the crystallite size, and a

variation in the ratio of the relative intensities of XRD peaks are observed. For longer milling times the broadening of the peaks and changes in the intensity ratio of the peaks does not vary noticeably. These changes can be ascribed to a slight decrease of the crystallinity and/or to a modification of the crystallite morphology as confirmed by SEM (Figure SI3), while no changes are detected in the background which could evidence the possible amorphization of a large portion of the sample. Indeed, based on the average domain size extracted from Le Bail refinements (Table SI1), the crystallite size varies from 30 to 15 nm from 3 to 12 h of ball milling, respectively.

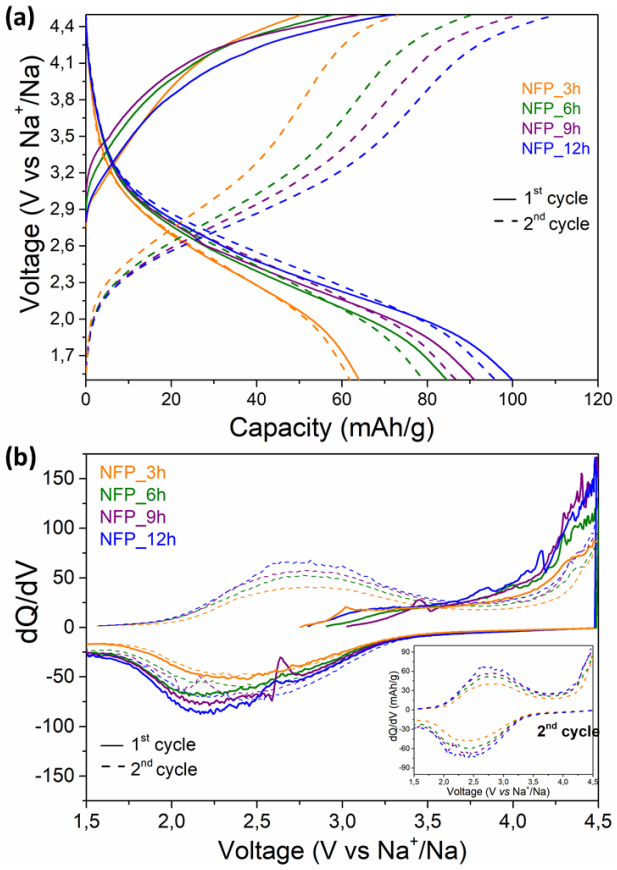

Figure 4. *Effect of the ball milling time in (a) the galvanostatic charge/discharge and (b) CV curves for the first two cycles.*

The drastic impact of the milling time on the capacity was evaluated by electrochemical characterization in half-cell configuration vs. Na metal, as shown in Figure 4a. An increase of milling time leads to larger charge and discharge capacities, progressively increasing the discharge capacity from 13 mAh g^{-1} for sample NFP_0h to 100 mAh g^{-1} to sample NFP_12h. In the cyclic voltammetry sweeps, only the reversible oxidation and reduction peaks of the Fe^{3+}/Fe^{2+} redox couple are clearly visible, although strongly broadened (Figure 4b). Table SI2 summarizes the capacity values achieved for the first charge and the first discharge cycles. Interestingly, all milled samples exhibit a considerable extra capacity in the first discharge (which is retained in subsequent charge and discharge cycles) representing at least 30% of the first charge

capacity and reaching 46% of the theoretical capacity in sample NFP_12h. This extra-capacity observed after ball milling is typical of ball milled NFP samples [12,14,28]. Mössbauer spectroscopy measurements were carried out to better understand the evolution of the oxidation state of Fe in the milled samples (Figure 5). The obtained results (Table SI2) indicate that, contrary to the pristine sample (NFP_0h, see Figure SI2), all ball-milled samples contain a significative amount of Fe^{3+}, which increases with the milling time (from 17 to 37%, varying the milling time from 3 to 12 h, respectively). This indicates that the samples are partially oxidized after ball-milling with C65, and explains why the first charge (presumably associated to the oxidation of Fe^{2+} into Fe^{3+}) is significantly shorter than the subsequent discharge. It is noteworthy that, in spite of the reducing character of carbon, the ball milling process leads to the formation of the same amount of Fe_{3+} whatever it is carried out under air or under neutral atmosphere of Argon (Figure SI6 and Table SI3).

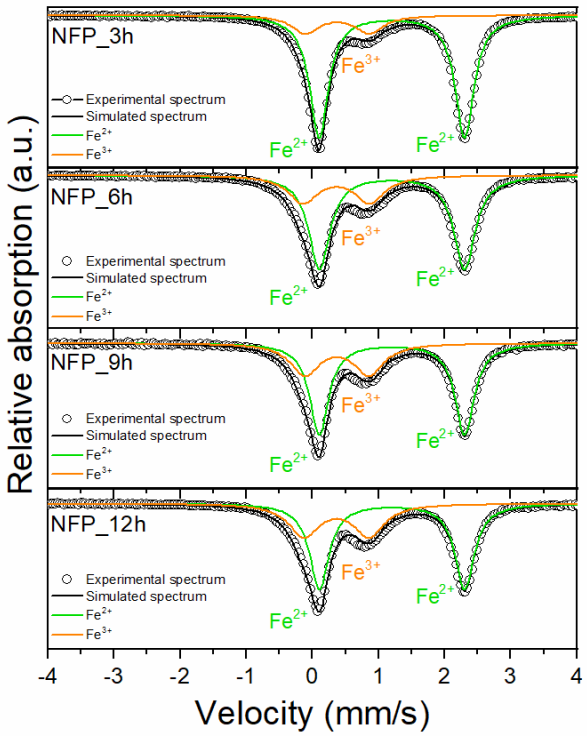

Figure 5. *Mössbauer spectra at different ball milling times (3h, 6h, 9h, 12h).*

Raman spectroscopy was also used to study the effect of ball milling on the maricite NFP particles (Figure SI7). The Raman spectra of the maricite samples may be considered as consisting of four distinct regions: region *(i)* between ca. 140 and 550 cm^{-1} , which is complex but generally dominated by Fe-O and network bending modes; region *(ii)* between ca. 550 and 900 cm^{-1}, which is associated with P-O bending modes; region *(iii)* between ca. 900 and 1100 cm^{-1}, which relates to P-O stretching modes; and region *(iv)* between ca. 1100 and 1800 cm^{-1}, where the two signals at ca. 1347 and 1586 cm^{-1} may be attributed to the D and G bands of carbon (when present). After

three hours of ball milling, most of the P-O stretching modes in region *(iii)* transform from sharp and well-defined peaks (NFP_0h) to a broad band (NFP_3h) reminiscent of that previously seen for amorphous/glassy iron phosphate-based materials [29,30]. At the same time, new bands appear in regions *(i)* and *(ii)*, implying the generation of new species [29,31]. Longer milling times result in the regular growth of the carbon-to-NFP signal, which indicates an increase of the carbon coverage, but no other significant spectral differences are detected after 9 hours of milling. By contrast, examination of the sample milled for 12 hours revealed a noticeable "shoulder" in region *(iii)* at ca. 970 cm^{-1} (C), as well as three additional peaks in region *(ii)* between 570 and 700 cm^{-1} (B), and a new peak in the region *(i)* at ca. 490 cm^{-1} (A). Given that these new peaks mainly associated with P-O stretching modes occur without the appearance of new crystalline phases in the XRD patterns (Figure 3), they are ascribed to the formation of new species lacking long-range order [28]. Finally, after 12 hours of ball milling, new peaks and shoulders appear in regions *(iii)* and *(iv)*, which are similar to those previously observed for P-O bonds in P_2O_7 dimers and isolated PO_4. These results (confirmed later by *ex situ* XAS and *operando* Mössbauer spectroscopy, *vide infra*) suggest that ball milling not only carbon coats the NFP particles, but also induces a mechanical degradation involving the formation of one or more sodium iron-phosphate/phosphate-based phases with low crystallinity.

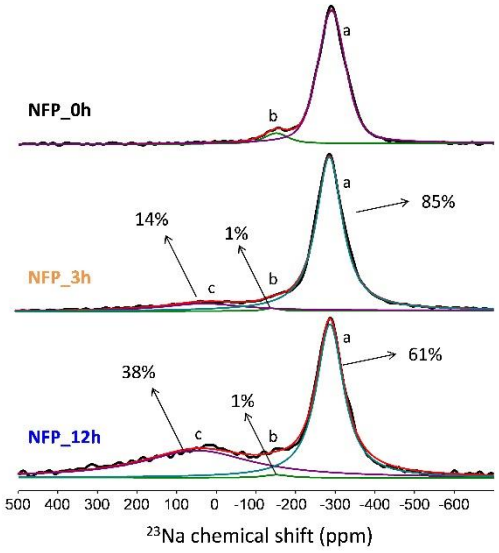

Figure 6. *^{23}Na solid state NMR spectrum of pristine NFP_0 and at 3h and 12h ball milling time.*

The previous findings were also confirmed by solid state NMR. In Figure 6, the ^{23}Na solid-state NMR spectra of maricite NFP are displayed for three different ball milling times (0h, 3h and 12h). The first spectrum corresponding to the pristine material (NFP_0h) is characterized by two resonances (signals a and b), where the minor signal b could be in principle ascribed to the anti-site defects of the structure. A new signal at higher ppms appear in the spectra of the ball-milled samples NFP_3h and NFP_12h.

The integration of broad NMR signals in paramagnetic solid-state NMR is not straightforward, as the total quantification should consider the intensities of the sidebands and their intensity can be distorted by pulse imperfections. Nevertheless, the presence of a new broad signal at around 50 ppm (signal c) is clear in the ^{23}Na NMR spectra of Figure 6 that increases as a function of the treatment time. The tentative deconvolution of this signal in NFP_12h (38% signal c) matches very well the concentration of Fe^{3+} (see Figure 5 and Table SI2), which might suggest the formation of a new sodiated-Fe^{3+} phase. In Figure SI8, the ^{31}P solid-state NMR spectra of the different maricite NFP samples are represented. They are centered at around 10700 ppm, which agrees with the very strong hyperfine shifts commonly observed in paramagnetic materials containing iron. No clear shifts are observed between the different ^{31}P spectra indicating that the main structure of the material is retained. The main difference observed is in the line broadening as the ^{31}P NMR signals, that are clearly less defined in NFP_12h. This is assigned to a larger number of defects. In conclusion, from the NMR data, we observe that the pristine material overall retains its structure although exhibits lower crystallinity upon ball-milling as it can be observed in the ^{31}P solid state NMR spectra, which agrees with the Raman conclusions. Also, an additional phase is formed upon ball milling as observed by the ^{23}Na spectra and its population increases upon ball milling time. This new phase (either forming at the surface, or appearing as a separate compound) still contains Na ions and its concentration is in agreement with the Fe^{+3} amount measured by Mössbauer spectroscopy. No additional NMR signals of ^{31}P are observed for this new phase but ^{31}P signals are broad in paramagnetic materials and therefore low amounts of P environments might not be visible in the spectra.

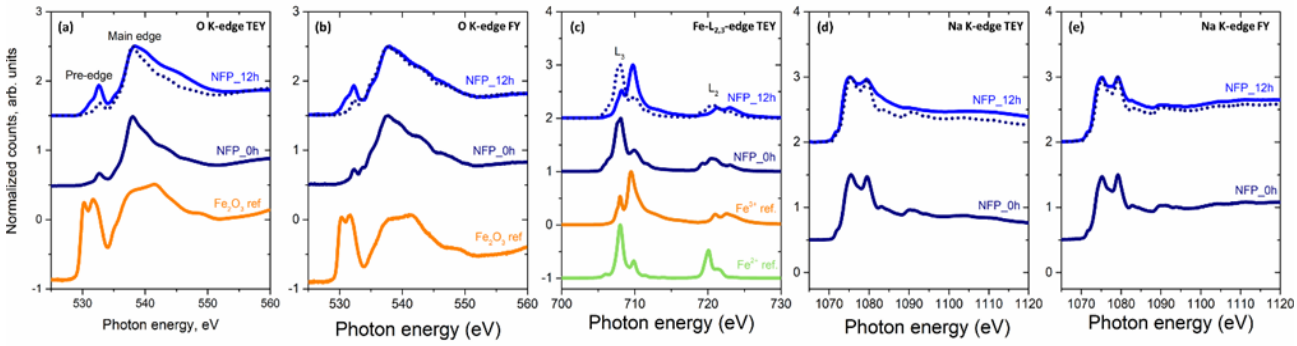

Figure 7. *XAS of pristine maricite NFP_0h and NFP_12h. XAS characterization at O K-edges (a, b), Fe L-edges (c), and Na K-edges (d, e). Both electron (TEY) and fluorescence (FY) modes of detection were shown. Fe L_3 suffered self-absorption in fluorescence detection mode and is not shown. The dotted line corresponds to the spectra of the pristine powder (NFP_0h).*

The XAS spectra of the O K-, Fe $L_{2,3}$-, and Na K-edges of the pristine maricite NFP (NFP_0h) and milled NFP powder (NFP_12h) are shown in Figure 7. The features of the O K-edge XAS spectra represent electronic transitions from the filled O 1s to the empty 2p orbitals [32,33]. In these spectra (Figure 7a and 7b), two regions can be

distinguished: *(i)* the pre-edge region (< 535 eV) corresponding to O 2p orbitals hybridizing with empty Fe 3d states and *(ii)* the main edge region (> 5 triphylite 35 eV), corresponding to the O 2p orbitals hybridizing with empty 4p states of Na, Fe and P [34]. And, despite the spectra being dominated by the signal of PO_4 in the main edge region, absorption events in the pre-edge region provide evidence of covalent metal-ligand bonding. The O K-edge spectrum of the pristine powder (NFP_0h) is in good agreement with previous measurements of maricite $NaFePO_4$ [15]. In the spectrum collected in the TEY mode, there is a single pre-edge peak at 532.6 eV and a single main edge feature with a peak maximum at 538 eV (Figure 7a). In FY mode, there are two pre-edge peaks at 532.3 and 533.7 eV and the sp peak at 538 eV (Figure 7b). In the TEY spectrum of the ball milled sample (NFP_12h), the pre-edge signal broadens and a new peak appears at 531.4 eV, which is consistent with the generation of holes in the Fe 3d-band and thus with the oxidation of Fe^{2+} to Fe^{3+} during ball milling. The changes were similar in both electron and fluorescence detection modes, suggesting that the oxidation of Fe^{2+} to Fe^{3+} occurs both at the surface and throughout the particle. In the Fe $L_{2,3}$ spectra, TEY mode (Figure 7c), the presence of two absorption regions was observed at approximately 709 and 722 eV. These regions present features which correspond to transitions from transition-metal $2p_{3/2}$ and $2p_{1/2}$ states to the unoccupied 3d states, L_3 and L_2 respectively. With respect to the L_3-edge, it is characterized by two absorption lines (708 and 710 eV) that differ in relative intensity depending on the oxidation state of Fe. The peak at 708 eV has a higher relative intensity in Fe^{2+} containing samples, such as FeO [35,36] and $LiFePO_4$ [37–40], which is expected for pristine NFP. Following ball milling, the absorption feature at 710 eV has relatively higher intensity; which provides more evidence that Fe_{2+} oxidized to Fe_{3+}, in agreement with the results of Mössbauer spectroscopy. The Na K-edge spectra correspond to the excitation of Na 1s electrons to empty 2p states. Both TEY and FY spectra of NFP_0h are very similar, indicating that the electronic states of Na are similar on the surface and in the bulk of the material (Figure 7d and 7e). The relative intensity of the absorption bands is similar to that of maricite $NaFePO_4$ reported by Xiong *et al* [15]. Upon ball milling (NFP_12h), the three spectral features between 1070 and 1080 eV of NFP_12h remain similar to those of NFP_0h, suggesting that the nearest coordination environment of Na is maintained after ball-milling treatment. However, the spectral features above 1080 eV are lost in the TEY mode, indicating the formation of a disordered surface layer with low crystallinity, as previously observed in the literature [15]. Interestingly, these features are not lost in the FY spectra but only reduced in intensity, indicating that the maricite structure is better retained in the inner part of the particles.

In summary, by combining the results of XRD, SEM, Raman, Mössbauer spectroscopy, ssNMR and XAS, it has been shown that ball milling with carbon results in a material with at least two different species, once consisting of crystalline maricite NFP with smaller crystallite size and a second species, possibly located at the surface of the first

one, presenting a more disordered nature and cointaining Fe (mainly as Fe^{3+}), Na and most likely also P (Scheme 1). Our hypothesis is that it is similar to partially oxidized maricite at the local scale. This would be in agreement with the electrochemical curve where only a very small portion of the capacity is attributed to the crystalline maricite NFP, and assigning the observed extra-capacity to new phases formed mainly at the surface of the particles upon ball milling, which will be discussed in the next section.

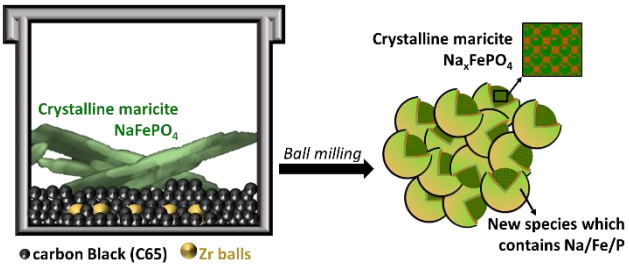

Scheme 1. *Schematic illustration of the ball milling effect on crystalline stick shaped NFP. The ball milling with C65 leads to a crystalline NFP with smaller size and the formation of new more disordered species possibly located at the surface.*

For comparison, a carbon-coated maricite NFP sample (*cc-m-* NFP, as it is known to be the thermodynamically stable phase) prepared by heat treatment at 500°C for 6h of carbon-coated triphylite (*cc-t*-NFP), without undergoing ball milling, was studied in order to ensure that the activation of maricite NFP can only be triggered by the ball milling with carbon (see details in the supplementary information, (Figure SI4). Figure SI5 shows the first charge and discharge curve of such carbon coated maricite NFP. The limited obtained capacity confirms that even though maricite NFP has a homogeneous carbon coating, it is the ball milling with carbon which activates the electrochemistry response of the maricite NFP.

Reaction mechanism of NFP_12h

The reaction mechanism of the maricite sample with the highest reversible capacity (NFP_12h) was studied in more detail to understand the possible contributions of crystalline NFP and of the new species formed at the surface of the particles during ball milling. *Operando* SXRD measurements, accompanied by *ex situ* and *operando* spectroscopy measurements at the surface (XAS) and in the bulk (XAS and Mössbauer) at different states of charge and discharge were carried out. The evolution of the o*perando* SXRD patterns during the first galvanostatic cycle of NFP_12h vs. Na is depicted in Figure 8. Surprisingly, contrary to the claims of many previous publications, the sample remains crystalline throughout the whole process [12,13,16,17]. However, while the same crystal structure is retained through the oxidation process, a slight shift in peak positions and modification of the intensity is observed, as highlighted in the zoomed area. These changes testify a slight variation of the *a* and *c* cell parameters as well as of the Na occupancy, in line with the deinsertion of Na^+ ions from the maricite structure (Figure 8c). The cell parameters obtained from the Rietveld refinement of the

first SXRD pattern, which corresponds to open circuit voltage (OCV) conditions, are *a* = 8.9966(3) Å, *b* = 6.8607(3) Å and *c* = 5.0451(2) Å, in agreement with those obtained for the pristine material (Figure SI9 and Table SI4), and for the pristine ball milled NFP_12h sample (Table SI2). At the end of the charge, the unit cell parameters are *a* = 8.9923(6) Å, *b* = 6.8626(6) Å and *c* = 5.0434(4) Å with a composition of $Na_{\approx 0.85}FePO_4$ (only ~0.15 Na^+ removed). These results indicate that crystalline maricite NFP contributes only to 15% of the total capacity, which corresponds to only ~20 mAh g^{-1} (in agreement with

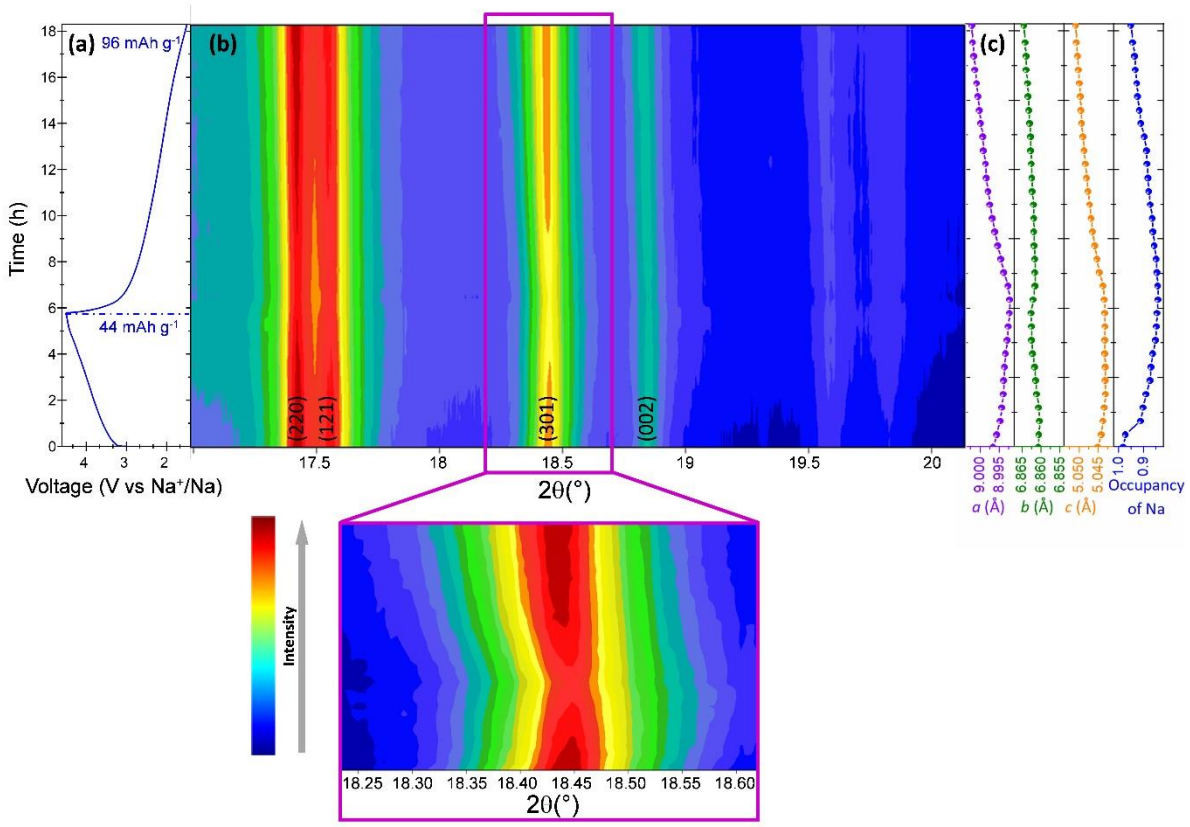

Figure 8. *(a) Voltage versus time curve of operando synchrotron of NFP_12h, (b) selected region of 2D-plot of 2ϑ versus time of the XRD patterns comprising the first full charge and discharge (warmer color indicates the more intense peaks) and (c) evolution of the unit cell parameters and occupancy along the full cycle.*

figure 2, no ball milled maricite NFP_0h) and attribute an extra-capacity of around ~25 mAh g^{-1} (total capacity at end of charge ~44 mAh g^{-1}, see Figure 8) to the new species with lower crystallinity generated by ball milling, in agreement with previous Raman, ssNMR and XAS results (*vide supra*). During the discharge process, the peaks are shifted to lower angles, corresponding to a slight increase of the cell parameters (*a* = 9.0022(7) Å, *b* = 6.8609(6) Å and *c* = 5.0509(5) Å) and of the sodium occupancy, $Na_{\approx 0.97}FePO_4$, suggesting that the limited Na^+ insertion/deinsertion process is reversible in the crystalline maricite NFP. The unit cell parameters continuously evolve along the electrochemical process, also evidencing that the contribution of crystalline maricite NFP to the capacity is continuous throughout cycling. This means that crystalline maricite NFP and other more disordered species that contains Fe^{+3} produced by ball

milling (previously observed by Raman, ssNMR, XAS, etc.), simultaneously contribute to the total capacity.

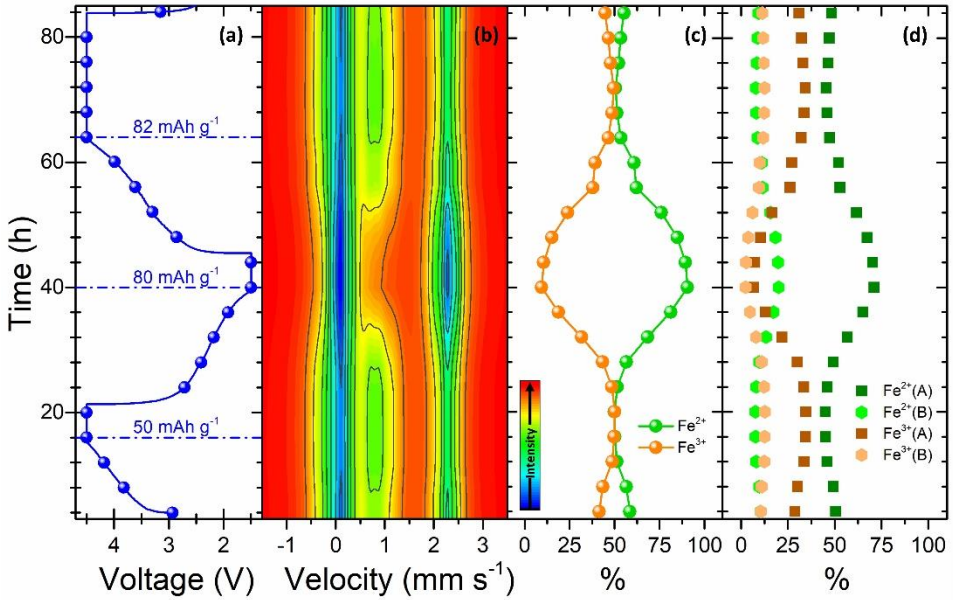

Figure 9. *(a) Voltage versus time curves of operando Mössbauer experiment of NFP_12h, (b) 2D-plot of the evolution of the Mössbauer spectra during cycling (c) evolution of the percentage of Fe^{2+} and Fe^{3+} (d) evolution of the different component of Fe during cycling measured by operando Mössbauer Spectroscopy. Note: Fe^{2+} (A): equivalent to M1 in maricite Na_xFePO_4; Fe^{2+} (B): equivalent to M2 in triphylite Na_xFePO_4; Fe^{3+} (A): equivalent to M1 in maricite Na_xFePO_4; Fe^{3+} (B): equivalent to M2 in triphylite Na_xFePO_4 or heterosite $FePO_4$.*

Operando ^{57}Fe Mössbauer spectroscopy allows following in detail the evolution of the iron oxidation state during cycling. The full *operando* dataset was first analysed by PCA, which showed that at least two independent components are necessary to explain the observed evolution of the spectra. Based on these results, the MCR-ALS analysis provided two pure components, which were then fitted as common Mössbauer spectra (Table 1). This evolution together with the corresponding voltage versus time curves are shown in Figure 9, and Table SI5 summarizes the fitted Mössbauer parameters for the two MCR-ALS pure component. MCR-ALS component #1 can be fitted with two spectral contributions, both attributed to divalent iron (Fe^{2+}). MCR-ALS component #2, on the other hand, contains at least three subspectra, two with the typical parameters of trivalent iron (Fe^{3+}) and one practically identical to the most intense subspectrum in MCR-ALS component #1, (Fe^{2+}). These data suggest the presence of a distribution of several non-equivalent Fe^{2+} and Fe^{3+} species, which are in line with the formation of new species with some degree of disorder during ball milling (see previous section), as it was suggested by Xiong *et al* [15]. In particular, these comprise one Fe^{2+} component, named Fe^{2+}(A), typical of Fe^{2+} occupying the M1 site in maricite Na_xFePO_4, and a second one equivalent to the typical Fe^{2+} occupying the M2 in triphylite Na_xFePO_4 [41] Trivalent iron (Fe^{3+}) is also observed in two different components: the component Fe^{3+}(A) which corresponds to the Fe^{3+} contained in the

oxidised form of maricite, and Fe^{3+}(B) which is equivalent to the Fe^{3+} occupying M2 site in the triphylite Na_xFePO_4 or heterosite $FePO_4$. It is important to point out that this refers to the local environment of the iron centres and not to the presence of these crystalline phases. During the whole process, about 75-80 % of the total iron (Fe^{2+} and Fe^{3+}) is always contained in the M1 site equivalent to maricite, whether it has long range order or not (dark green and dark brown squares in Figure 9) [14,42,43]. At OCV (Figure 9c), the total Fe^{2+} (A+B) is 61 % (in agreement with the Mössbauer measurements at NFP_12h, see Table SI2), which limits the charge capacity attributed to Na^+ extraction in the first cycle. After the first charge step to 4.5 V, only part of the Fe^{2+} is oxidized reaching final ratio of Fe^{2+}:Fe^{3+} of about 1:1. Both Fe^{2+} (A) and Fe^{2+} (B) contribute to a fraction (28%, 14 mAh g^{-1}) of the observed capacity (50 mAh g^{-1}), which indicates that most of the capacity may be attributed to irreversible processes or to surface (non-faradaic) activity (see below, *ex-situ* XAS measurements, for more information) [18,19] The contribution of the irreversible processes or to surface activity during this first charge is more noticeable by Mössbauer than by XRD, which can be due to the differences in the electrode preparation process for the two techniques. After the following discharge to 1.5 V, almost the totality of the Fe^{3+} is reduced to Fe^{2+}, only remaining a 9% as Fe^{3+}, with a capacity of 80 mAh g^{-1}. About 75% of this capacity (60 mAh g^{-1}) can be explained by the total Fe^{3+} reduction to Fe^{2+}, confirming that ball milling efficiently activates the material producing a notable increase in capacity, generating new disorder species that contains both Fe^{2+} and Fe^{3+} leading to higher discharge capacity and showing good reversibility. This was confirmed after the second charge at 4.5 V, observing that the total Fe^{3+} increased up to 50%, with a capacity of 82 mAh g^{-1} and a relatively high coulombic efficiency >98%.

Table 1. *Mössbauer hyperfine parameters of the MCR-ALS pure componentes*

MCR-ALS component	Subspectrum	δ (mm·s^{-1})	Δ (mm·s^{-1})	Γ (mm/s)	Area (%)	Active material/species
#1	Fe^{2+}(A)	1.19(1)	2.26(1)	0.36(1)	77(5)	Na_xFePO_4 (Fe^{2+} in M1 equivalent to maricite)
	Fe^{2+}(B)	1.14(1)	1.88(4)	0.41(4)	23(5)	Na_xFePO_4 (Fe^{2+} in M2 equivalent to triphylite)
#2	Fe^{2+}(A)	1.21(1)	2.20(1)	0.30(2)	29(1)	Na_xFePO_4 (Fe^{2+} in M1 equivalent to maricite)
	Fe^{3+}(A)	0.38(1)	0.82(2)	0.45(3)	52(5)	Na_xFePO_4 (Fe^{3+} in M1 equivalent to maricite)
	Fe^{3+}(B)	0.37(1)	1.42(5)	0.42(5)	19(5)	$Na_xFePO_4/FePO_4$ (Fe^{3+} in M2 equivalent to triphylite/heterosite)

From the combination of the *operando* SXRD and Mössbauer spectroscopy, it can be concluded that during cycling 75% of the capacity is attributed to the redox activity of iron and 25% is attributed to irreversible processes or to surface (non-faradaic) activity. In parallel, 15% of the capacity involves Na^+ insertion/extraction from crystalline maricite occurring simultaneously with the aforementioned redox activity of the iron.

Ex situ XAS was performed on cycled electrodes prepared following two different routes: (1) a first series of samples was prepared by starting with a charge process (Figure 10) and (2) a second one by starting in discharge (Figure 11). For the first series, the samples were first charged to 4.5 V and then discharged to 1.5 V vs. Na^+/Na for two cycles. During the first charge (from point 1 to 3, Figure 10a), in the O K-edge spectra, the pre-edge feature near 531 eV, which correspond to O 2*p* orbitals hybridizing with empty Fe 3*d* states [33,34,44–46] decreases in intensity, while a new one appears at 534 eV during the discharge (Figure 10b). The decrease of this signature at low energy is a sign of filling holes in the valence band, which is consistent with Fe^{3+} reduction, as observed in the Mössbauer experiments (Figure 9). Following the discharge step (from point 3 to 5, Figure 10a), the O K-edge spectra become similar to that of pristine $NaFePO_4$, indicating a reduction of Fe^{3+} to Fe^{2+}. These modifications during charge and discharge are observed in both TEY and FY modes, suggesting that the reduction of Fe^{3+} to Fe^{2+} occurs both at the surface and in the bulk of the particles. In the second cycle, a new absorption peak emerges around 545 eV only in the spectrum measured in the TEY mode, indicating that new O-based species are formed mainly at the surface of the particles. In the Fe $L_{2,3}$-edge spectra (Figure 10b), no significant changes occur during charge, but the absorption line at 708 eV gets more intense during the following discharge. At the same time, the feature at 710 eV decreases in intensity, suggesting the complete reduction of surface Fe^{3+} to Fe^{2+}, in agreement with Mössbauer spectroscopy [35–39]. In the second cycle, spectra similar to the fully charged (3) and fully discharged states (5) are obtained, indicating that the

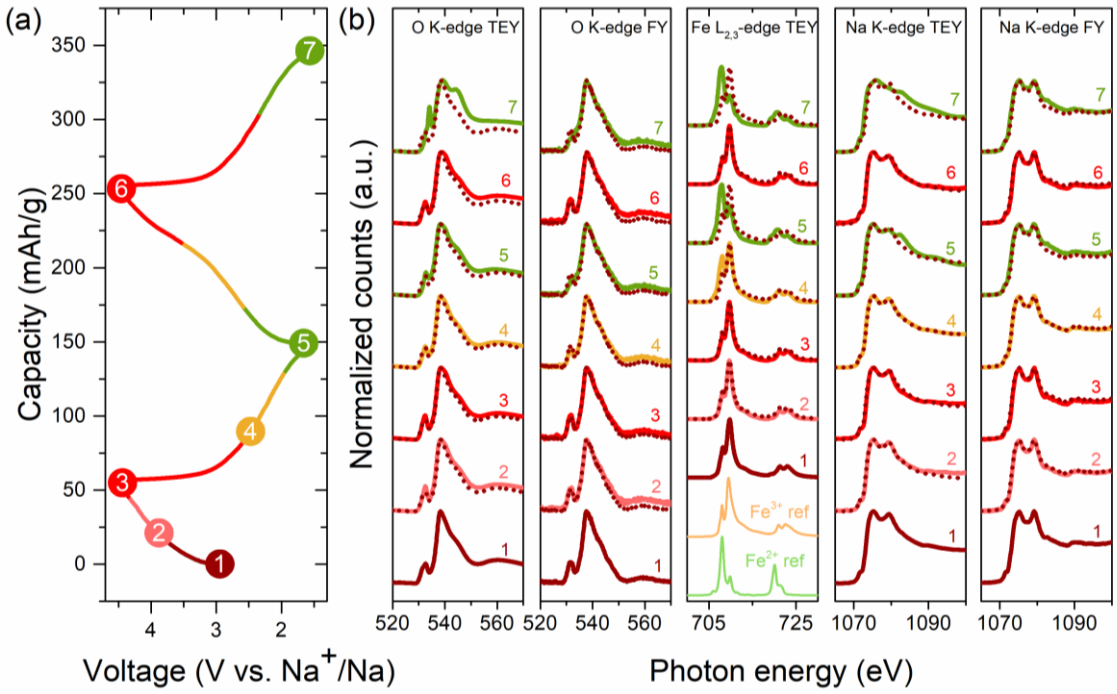

***Figure 10**. (a) Galvanostatic charge and discharge curves of NFP_12h and (b) both electron and fluorescence modes of O K-edges, Fe $L_{2,3}$-edges, and Na K-edges. Fe L_3 suffered self-absorption in fluorescence detection mode and is not shown. The dotted line corresponds to the spectra of NFP_12h at point 1 (OCV).*

changes in the oxidation state of the iron at the surface are reversible, which support our findings that there is contribution of other non-crystalline species at the surface of the particles. Similarly in the Na K-edge XAS spectra, significant changes are observed in TEY detection mode, and only after the first discharge, where the main edge shifts slightly to lower energies and a new peak appears at 1083 eV. This suggests the formation of distinct Na species not seen in crystalline maricite $NaFePO_4$ during cycling. All these changes are reversible during the two cycles, those of the iron species in full agreement with Mössbauer results. The emergence of new features in the O K- and Na K-edge spectra also agree with the Mössbauer results. These additional absorption lines also become evident at the end of the second discharge in the Na K-edge spectrum measured in FY mode. Even though the lines are less intense than in the TEY spectrum, their presence indicates that the bulk of the particle contributes to this effect.

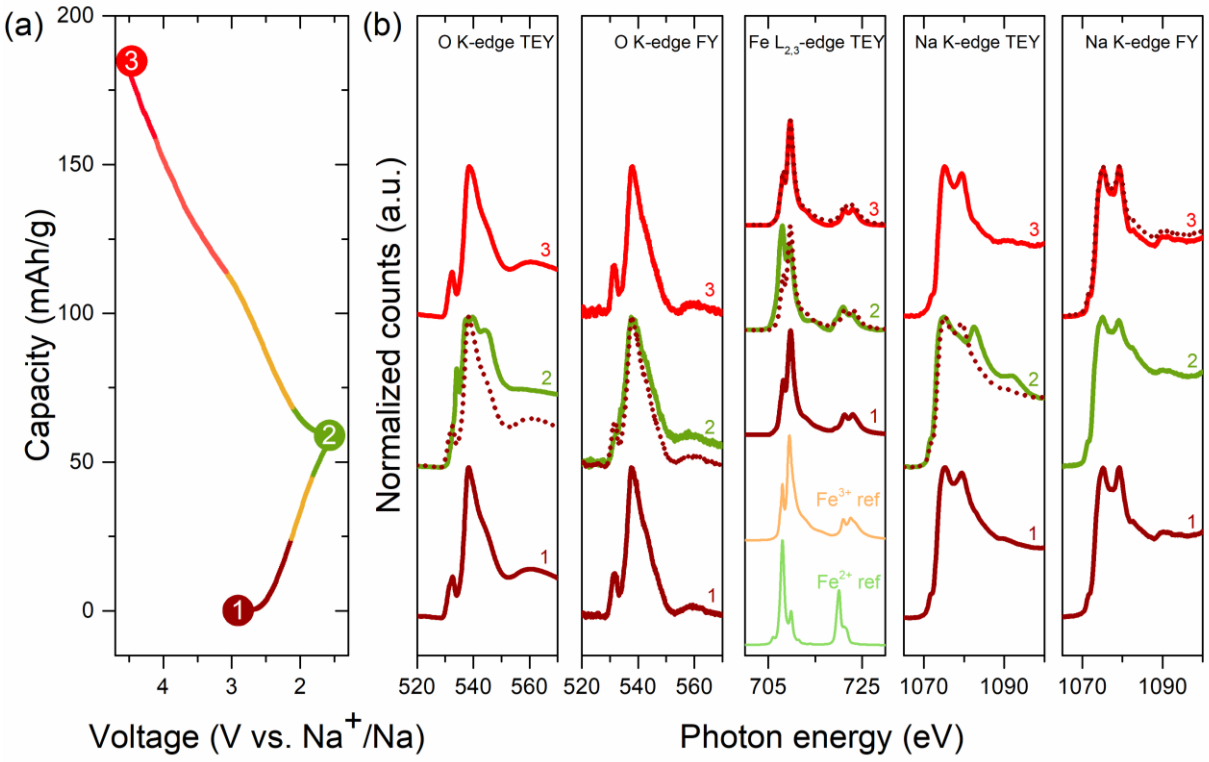

Figure 11. *(a) Galvanostatic discharge and charge curve of NFP_12h and (b) both electron and fluorescence modes of O K-edges, Fe $L_{2,3}$-edges, and Na K-edges. Fe L_3 suffered self-absorption in fluorescence detection mode and is not shown. The dotted line corresponds to the spectra of NFP_12h at point 1 (OCV).*

In the second series, the samples were prepared by first discharging them to 1.5 V and then charging to 4.5 V vs. Na^+/Na for 1 cycle (Figure 11a). In the O K-edge XAS spectra measured at the end of the discharge in the TEY mode, the pre-edge peak at 531 eV disappears and a new feature form at 534 eV (Figure 11b), in line with the changes seen following the first discharge in the first series. At the same time, the main

absorption edge broadens and additional peaks become evident. This is consistent with the reduction of Fe and the formation of new iron species at the surface. These modifications are less evident but still subsist in the spectrum measured in the FY mode, indicating that the modifications mainly concern the surface of the particles. Upon charging, the spectrum becomes very similar to that of the pristine material, indicating that the changes are reversible. The Fe $L_{2,3}$-edge spectra evolution during a cycle when the electrode is first completely discharged shown in Figure 11b indicate that the Fe located on the surface is reduced to Fe^{2+}. Then, the electrode is charged and the spectra change returning to the original pristine electrode shape, indicating again full reversibility. Similar reversible modifications are observed in the Na K edge spectra, with new spectral features appearing at the end of the discharge at 1082 and 1092 eV mainly in the TEY spectrum, suggesting that the possible formation of reversible new species occurs predominately at the surface of the material.

Therefore, the results obtained from the XAS analysis are consistent with the SXRD and Mössbauer spectroscopy, and also show that the surface of the ball milled particles is highly electrochemically active in contrast to the bulk.

Conclusions

A multimodal approach was employed to understand the effect of ball milling on the structure and the performance of maricite $NaFePO_4$ during (de)sodiation *vs.* Na metal. After ball milling of maricite with carbon, the relative amount of Fe^{3+} increases from 0 to 37 %. Moreover, ball milling produces a mixture of crystalline maricite $NaFePO_4$ located mostly in the bulk and partially oxidized species of lower crystallinity both at the surface and in the bulk of the ball milled particles. During cycling, and only a small fraction of Na^+ (x = ~0.15, corresponding to 15% of the total capacity) is reversibly extracted from the bulk crystalline maricite $NaFePO_4$. New species formed during ball milling, with low crystallinity and mainly located on the surface of the particles, show a considerably higher electrochemical contribution to the total capacity and good reversibility. 75% of the total capacity is attributed to Fe^{3+}/Fe^{2+} redox activity, mostly attributed to the active species mainly located on the surface of the material particles. The remaining 25% extra-capacity does not seem to be related to Fe^{3+}/Fe^{2+} activity, but rather to non-faradaic processes, associated to the new species formed during ball milling. Finally, it should be noted that in contrast to the previously reported literature, our findings show that there is no amorphization upon cycling.

Author Contributions

C. B and M. T. S. – investigation, conceptualization, validation, writing – original draft, writing-review and editing, A. J. F. R, J. M. L., J. S. G., L. N., E. D and G. N. – investigation, validation, writing – original draft, writing – review and editing, N. B. – experimental, validation, M. R. – funding acquisition, writing – original draft, writing – review and editing M. C. C – supervision writing – original draft, writing – review and editing and M. G – supervision, funding acquisition, writing – original draft, writing – review and editing. The manuscript was written through contribution from all authors. All authors have given approval to the final version of the manuscript.

Acknowledgements

The authors would like to acknowledge the MCIN/AEI/10.13039/501100011033 for the financial support through project PID2019-107468RB-C22, PID2019-106519RB-I00, as well as Project PLEC2021-007929 funded by MCIN/AEI/10.13039/501100011033 and by "ERDF A way of making Europe", by the "European Union" and by the "European Union NextGenerationEU/PRTR. The authors thank the French National Research Agency for its **II** nancial support through the Labex STORE-EX Labex Project ANR-10LABX-76–01. The "R´eseau des Rayons X et Gamma" (Univ. Montpellier, France) is gratefully thanked for granting access to their XRD and Mössbauer spectroscopy platform. Computational. Several experiments were performed at MSPD and BOREAS beamlines at ALBA Synchrotron with the collaboration of ALBA staff (experiments refs. 2016021599 and AV-2019093908). The authors would also like to thank F. Fauth and J. Herrero for experimental support and enriching discussions. The authors gratefully acknowledge K. Cavusogly for her lab-work assistance

Notes and references

[1] C. Berlanga, I. Monterrubio, M. Armand, T. Rojo, M. Galceran and M. Casas-Cabanas, *ACS Sustain. Chem. Eng.*, 2020, **8**, 725–730.
[2] G. Ali, J.-H. Lee, D. Susanto, S.-W. Choi, B. W. Cho, K.-W. Nam and K. Y. Chung, *ACS Appl. Mater. Interfaces*, 2016, **8**, 15422–15429.
[3] Y. Zhu, Y. Xu, Y. Liu, C. Luo and C. Wang, *Nanoscale*, 2013, **5**, 780–787.
[4] S.-M. Oh, S.-T. Myung, J. Hassoun, B. Scrosati and Y.-K. Sun, *Electrochem. Commun.*, 2012, **22**, 149–152.
[5] P. Moreau, D. Guyomard, J. Gaubicher and F. Boucher, *Chem. Mater.*, 2010, **22**, 4126–4128.
[6] M. Avdeev, Z. Mohamed, C. D. Ling, J. Lu, M. Tamaru, A. Yamada and P. Barpanda, *Inorg. Chem.*, 2013, **52**, 8685–8693.
[7] D. Saurel, M. Galceran, M. Reynaud, H. Anne and M. Casas-Cabanas, *Int. J. Energy Res.*, 2018, **42**, 3258–3265.
[8] M. Galceran, D. Saurel, B. Acebedo, V. V. Roddatis, E. Martin, T. Rojo and M. Casas-Cabanas, *Phys. Chem. Chem. Phys.*, 2014, **16**, 8837–8842.

[9] M. Casas-Cabanas, V. V. Roddatis, D. Saurel, P. Kubiak, J. Carretero-González, V. Palomares, P. Serras and T. Rojo, *J. Mater. Chem.*, 2012, **22**, 17421.
[10] K. Zaghib, J. Trottier, P. Hovington, F. Brochu, A. Guerfi, A. Mauger and C. M. Julien, *J. Power Sources*, 2011, **196**, 9612–9617.
[11] A. Sun, F. R. Beck, D. Haynes, J. A. Poston, S. R. Narayanan, P. N. Kumta and A. Manivannan, *Mater. Sci. Eng., B*, 2012, **177**, 1729–1733.
[12] J. Kim, D.-H. Seo, H. Kim, I. Park, J.-K. Yoo, S.-K. Jung, Y.-U. Park, W. A. Goddard III and K. Kang, *Energy Environ. Sci.*, 2015, **8**, 540–545.
[13] Y. Liu, N. Zhang, F. Wang, X. Liu, L. Jiao and L.-Z. Fan, *Adv. Funct. Mater.*, 2018, **28**, 1801917.
[14] R. Kapaev, A. Chekannikov, S. Novikova, S. Yaroslavtsev, T. Kulova, V. Rusakov, A. Skundin and A. Yaroslavtsev, *J. Solid State Electrochem.*, 2017, **21**, 2373–2380.
[15] F. Xiong, Q. An, L. Xia, Y. Zhao, L. Mai, H. Tao and Y. Yue, *Nano Energy*, 2019, **57**, 608–615.
[16] B. Liu, Q. Zhang, L. Li, L. Zhang, Z. Jin, C. Wang and Z. Su, *Chem. Eng. J.*, 2021, **405**, 126689.
[17] X. Ma, J. Xia, X. Wu, Z. Pan and P. K. Shen, *Carbon*, 2019, **146**, 78–87.
[18] B. Senthilkumar, K. V. Sankar, L. Vasylechko, Y.-S. Lee and R. K. Selvan, *RSC Adv.*, 2014, **4**, 53192–53200.
[19] M. Minakshi, D. Meyrick and D. Appadoo, *Energy Fuels*, 2013, **27**, 3516–3522.
[20] J. Rodríguez-Carvajal, *Phys. B*, 1993, **192**, 55–69.
[21] G. Grosse, *PC-Mos II, Version 1.0 Manual and Program Documentation*, 1993.
[22] R. A. Brand, *Normos Mössbauer Fitting Program*, Univ. Duisburg.
[23] J.-B. Leriche, S. Hamelet, J. Shu, M. Morcrette, C. Masquelier, G. Ouvrard, M. Zerrouki, P. Soudan, S. Belin, E. Elkaïm and F. Baudelet, *J. Electrochem. Soc.*, 2010, **157**, A606–A610.
[24] M. Fehse, A. Iadecola, M. T. Sougrati, P. Conti, M. Giorgetti and L. Stievano, *Energy Storage Mater.*, 2019, **18**, 328–337.
[25] D. Saurel, A. Pendashteh, M. J´auregui, M. Reynaud, M. Fehse, M. Galceran and M. Casas-Cabanas, *Chem.: Methods*, 2021, **1**, 249–260.
[26] J. N. Bridson, S. E. Quinlan and P. R. Tremaine, *Chem. Mater.*, 1998, **10**, 763–768.
[27] P. P. Prosini, C. Cento, A. Masci and M. Carewska, *Solid State Ionics*, 2014, **263**, 1–8.
[28] R. R. Kapaev, A. A. Chekannikov, S. A. Novikova, T. L. Kulova, A. M. Skundin and A. B. Yaroslavtsev, *Mendeleev Commun.*, 2017, **27**, 263–264.
[29] L. Zhang and R. K. Brow, *J. Am. Ceram. Soc.*, 2011, **94**, 3123–3130.
[30] L. Zhang, R. K. Brow, M. E. Schlesinger, L. Ghussn and E. D. Zanotto, *J. Non-Cryst. Solids*, 2010, **356**, 1252–1257.
[31] S. Nakata, T. Togashi, T. Honma and T. Komatsu, *J. Non-Cryst. Solids*, 2016, **450**, 109–115.
[32] E. I. Solomon, B. Hedman, K. O. Hodgson, A. Dey and R. K. Szilagyi, *Coord. Chem. Rev.*, 2005, **249**, 97–129.
[33] S. E. Shadle, B. Hedman, K. O. Hodgson and E. I. Solomon, *J. Am. Chem. Soc.*, 1995, **117**, 2259–2272.
[34] F. M. F. de Groot, M. Grioni, J. C. Fuggle, J. Ghijsen, G. A. Sawatzky and H. Petersen, *Phys. Rev. B: Condens. Matter Mater. Phys.*, 1989, **40**, 5715–5723.

[35] H. J. Lee, G. Kim, D. H. Kim, J.-S. Kang, C. L. Zhang, S.-W. Cheong, J. H. Shim, S. Lee, H. Lee, J.-Y. Kim, B. H. Kim and B. I. Min, *J. Phys.: Condens. Matter*, 2008, **20**, 295203.
[36] E. P. Domashevskaya, S. A. Storozhilov, S. Y. Turishchev, V. M. Kashkarov, V. A. Terekhov, O. V. Stognej, Y. E. Kalinin and S. L. Molodtsov, *J. Electron Spectrosc. Relat. Phenom.*, 2007, **156–158**, 180–185.
[37] M. H. Oh, T. Yu, S.-H. Yu, B. Lim, K.-T. Ko, M.-G. Willinger, D.-H. Seo, B. H. Kim, M. G. Cho, J.-H. Park, K. Kang, Y.-E. Sung, N. Pinna and T. Hyeon, *Science*, 2013, **340**, 964– 968.
[38] X. Liu, W. Yang and Z. Liu, *Adv. Mater.*, 2014, **26**, 7710–7729.
[39] T.-K. Sham, *Adv. Mater.*, 2014, **26**, 7896–7901.
[40] W. Yang, X. Liu, R. Qiao, P. Olalde-Velasco, J. D. Spear, L. Roseguo, J. X. Pepper, Y. Chuang, J. D. Denlinger and Z. Hussain, *J. Electron Spectrosc. Relat. Phenom.*, 2013, **190**, 64–74.
[41] N. V. Kosova, V. R. Podugolnikov, E. T. Devyatkina and A. B. Slobodyuk, *Mater. Res. Bull.*, 2014, **60**, 849–857.
[42] R. Amisse, M. T. Sougrati, L. Stievano, C. Davoisne, G. Drazici, B. Budic, R. Dominko and C. Masquelier, *Chem. Mater.*, 2015, **27**, 4261–4273.
[43] T. Fehr, R. Hochleitner, A. Laumann, E. Schmidbauer and J. Schneider, *Phys. Chem. Miner.*, 2010, **37**, 179–189.
[44] E. I. Solomon, B. Hedman, K. O. Hodgson, A. Dey and R. K. Szilagyi, *Coord. Chem. Rev.*, 2005, **249**, 97–129.
[45] F. Frati, M. O. J. Y. Hunault and F. M. F. De Groot, *Chem. Rev.*, 2020, **120**, 4056–4110.
[46] E. I. Solomon, B. Hedman, K. O. Hodgson, A. Dey and R. K. Szilagyi, *Coord. Chem. Rev.*, 2005, **249**, 97–129.